Inorg. Chem. **2008**, *47*, 2312−2324

Theoretical Studies on Structures and Spectroscopic Properties of Photoelectrochemical Cell Ruthenium Sensitizers, $[Ru(H_m tcterpy)(NCS)_3]^{n-}$ (m = 0, 1, 2, and 3; n = 4, 3, 2, and 1)

Ming-Xia Li,[†,‡] Xin Zhou,[†] Bao-Hui Xia,[†,§] Hong-Xing Zhang,[*,†] Qing-Jiang Pan,[‡] Tao Liu,[†] Hong-Gang Fu,[‡] and Chia-Chung Sun[†]

State Key Laboratory of Theoretical and Computational Chemistry, Institute of Theoretical Chemistry, and College of Chemistry, Jilin University, Changchun 130023, China, and College of Chemistry and Chemical Engineering, Heilongjiang University, Haerbin 150080, China

Received January 26, 2007

A series of ruthenium(II) complexes, $[Ru(tcterpy)(NCS)_3]^{4-}$ (**0H**), $[Ru(Htcterpy)(NCS)_3]^{3-}$ (**1H**), $[Ru(H_2tcterpy)(NCS)_3]^{2-}$ (**2H**), and $[Ru(H_3tcterpy)(NCS)_3]^{-}$ (**3H**) (tcterpy = 4,4′,4″-tricarboxy-2,2′:6′,2″-terpyridine), are investigated theoretically to explore their electronic structures and spectroscopic properties. The geometry structures of the complexes in the ground and excited states are optimized by the density functional theory and single-excitation configuration interaction methods, respectively. The absorption and emission spectra of the complexes in gas phase and solutions (ethanol and water) are predicted at the TDDFT(B3LYP) level. The calculations indicate that the protonation effect slightly affects the geometry structures of the complexes in the ground and excited states but leads to significant change in the electronic structures. In cases of both absorptions and emissions, the energy levels of HOMOs and LUMOs for **0H-3H** decrease dramatically as a result of the introduction of the COOH groups. The protonation much stabilizes the unoccupied orbitals with respect to the occupied orbitals. Thus, both the absorptions and emissions are red-shifted from **0H** to **3H**. The phosphorescence of **0H-3H** are attributed to tcterpyridine → d(Ru)/NCS (^{3}MLCT/^{3}LLCT) transitions. The solvent media can influence the molecular orbital distribution of the complexes; as a consequence, the spectra calculated in the presence of the solvent are in good agreement with the experimental results. The MLCT/LLCT absorptions of **0H** in ethanol and water are red-shifted relative to that in the gas phase. However, the MLCT/LLCT absorptions of the protonated complexes (**1H-3H**) are blue-shifted in ethanol and water with respect to the gas phase. Similarly, the solvent effect causes a blue-shift of the phosphorescent emission for **0H-3H**.

1. Introduction

In recent years, dye-sensitized solar cells (DSSCs) have attracted considerable interest for the conversion of sunlight into electricity because of their low cost and high efficiency.[1–4] Undoubtedly, one of the key components of these cells is the light-absorbing dye molecule that is used to sensitize the semiconductor electrode. To seek the effective sensitizers, a considerable number of systems have been synthesized and analyzed.[4–12] One of the most efficient sensitizing dyes is *cis*-dithiocyanato bis(2,2′-bipyridyl-4,4′-

* E-mail: zhanghx@mail.jlu.edu.cn.
† Institute of Theoretical Chemistry, Jilin University.
‡ Heilongjiang University.
§ College of Chemistry, Jilin University.

(1) O'Regan, B.; Grätzel, M. *Nature* **1991**, *353*, 737.
(2) Hagfeldt, A.; Grätzel, M. *Acc. Chem. Rev.* **2000**, *33*, 269.
(3) Grätzel, M. *Nature* **2001**, *414*, 338.
(4) Kalyanasundaram, K.; Grätzel, M. *Coord. Chem. Rev.* **1998**, *177*, 347.
(5) Nazeeruddin, M. K.; Kay, A.; Rodicio, I.; Humphry-Baker, R.; Müeller, E.; Liska, P.; Vlachopoulos, N.; Graetzel, M. *J. Am. Chem. Soc.* **1993**, *115*, 6382.
(6) Nazeeruddin, M. K.; Péchy, P.; Renouard, T.; Zakeeruddin, S. M.; Humphry-Baker, R.; Comte, P.; Liska, P.; Cevey, L.; Costa, E.; Shklover, V.; Spiccia, L.; Deacon, G. B.; Bignozzi, C. A.; Grätzel, M. *J. Am. Chem. Soc.* **2001**, *123*, 1613.
(7) Zakeeruddin, S. M.; Nazeeruddin, M. K.; Humphry-Baker, R.; Péchy, P.; Quagliotto, P.; Barolo, C.; Visvardi, G.; Grätzel, M. *Langmuir* **2002**, *18*, 952.
(8) Nazeeruddin, M. K.; Angelis, F. D.; Fantacci, S.; Selloni, A.; Viscardi, G.; Liska, P.; Ito, S.; Taleru, B.; Grätzel, M. *J. Am. Chem. Soc.* **2005**, *127*, 16835.
(9) Wang, Z.-S.; Yamaguchi, T.; Sugihara, H.; Arakawa, H. *Langmuir* **2005**, *21*, 4272.

10.1021/ic070139b CCC: $40.75
Published on Web 02/27/2008

dicarboxylate) ruthenium(II) complex,[5,7–10,13] known as N3 or red dye, for which the incident photon to current conversion efficiency (IPCE) value is nearly 80% in the range of 400–600 nm. However, the main drawback of N3 is the lack of absorption in the red region of the visible spectrum. Numerous attempts to synthesize more superior sensitizers[14–18] failed to improve the efficiency and to enhance the spectral response in the red and infrared region until 1997. Then, Grätzel and co-workers[19] synthesized a series of panchromatic terpyridine Ru(II) complexes, $[Ru(tcterpy)(NCS)_3]^{4-}$(**0H**), $[Ru(Htcterpy)(NCS)_3]^{3-}$(**1H**), $[Ru(H_2tcterpy)(NCS)_3]^{2-}$ (**2H**), and $[Ru(H_3tcterpy)(NCS)_3]^{-}$ (**3H**) (tcterpy = 4,4′,4″-tricarboxy-2,2′:6′,2″-terpyridine), which show absorptions in the visible region and extending to the near-IR region up to 920 nm, yield over 80% IPCE, and produce an overall efficiency of 10.4%.[6,19]

As the dye sensitizer, the following qualities are of vital importance. First, the sensitizer molecules should exhibit absorptions in a broad range of visible light. Second, the excited state of the sensitizer should match the conduction band of the TiO_2. Third, the sensitizer must show high thermal stability. Furthermore, the presence of terminal acidic carboxylic groups in the sensitizer usually allows stable anchoring of the sensitizer to the semiconductor surface, so as to ensure a high electronic coupling between the dye and the semiconductor, which is required for efficient charge injection. All of these factors are closely associated with the ground and excited states of the sensitizers. Moreover, the spectroscopic properties and electron structures of the dye are crucial in determining the long-term stability, the light harvesting efficiency of the DSSC device, and charge-transfer dynamics at the semiconductor interface.[14,15] Therefore, it is of practical importance to explore the electron structures of the sensitizer and to investigate its excited states and the behavior on the dye−semiconductor interface.

The black dye containing different degrees of protonation (**0H**−**3H**) has been fully characterized by Grätzel and co-workers.[6,19–21] A ethanolic solution of the four complexes (**0H**−**3H**) show lower-energy MLCT absorption at 590, 610, 620, and 625 nm, respectively. Grätzel has tentatively assigned the absorptions of the four complexes in the visible region to metal to ligand charge transfer (MLCT) transitions and those in ultraviolet region to $\pi \rightarrow \pi^*$ electron transition. In particular, the absorption spectra of the black dye in ethanol show pH dependence and are red-shifted with the decrease of the pH from 11 to 5.0, to 3.3, and to 2.2. The four kinds of acidic condition correspond to the four protonation form of the molecule, that is, the full deprotonated form (**0H**), monoprotonated form (**1H**), diprotonated form (**2H**), and fully protonated form (**3H**), respectively. Complexes **0H**, **1H**, **2H**, and **3H** in ethanol solution show luminescence at 820, 854, 900, and 950 nm, respectively, and the observed emissions of **0H**−**3H** have been attributed to originate from the Ru(tcterpy) CT excited state.[6] Furthermore, both the emission wavelength and lifetime of the black dye exhibit pH dependence, and the emissions show a red-shift with the increase of the solution acidicity. Apparently, varying the degree of protonation of the black dye introduces changes in its electronic structure, so that it is important to explore the electronic structures of the dye in the ground and the excited states at different acidic condition.

In contrast to numerous experimental studies, only a few theoretical calculations have been performed for the black dye molecules.[22,23] Aiga and co-workers have characterized the molecular and electronic structures of the fully protonated black dye complex, which was limited to the gas phase, by density functional theory (DFT) calculation with PBE0 functional.[22] Very recently, another theoretical investigation focused on the ground-state properties (such as energies, geometries, and population analysis in molecular orbitals) and the absorption spectra of the fully protonated black dye complex and its linkage isomers. However, to date, no detailed theoretical studies have focused on the following matter: (1) the geometry and electronic structures of the black dye in the excited states, (2) emission spectra, (3) protonation effect, and (4) solvent effect and solvatochromism. Thus, as resported in this paper, we employed DFT, the single-excitation configuration interaction (CIS) method, and time-dependent density functional theory (TDDFT) to study the geometry and electronic structures of the black dye in both ground and excited states, the absorption and emission spectral properties, and solvatochromism properties. In particular, we have extensively investigated protonation effect of the terminal carboxylic groups on the geometry, electronic structures, and the optical properties of the black dyes. The solvent effects are seriously considered using the conductor-like polarizable continuum model (CPCM). These results will provide a direct insight into the origins of the observed transitions and their possible role in dye-sensitized solar cell injection dynamics, as well as the design of new and more efficient solar cells sensitizers.

(10) Barolo, C.; Nazeeruddin, M. K.; Fantacci, S.; Censo, D. D.; Comte, P.; Liska, P.; Viscard, G.; Quagliotto, P.; Angelis, F. D.; Ito, S.; Grätzel, M. *Inorg. Chem.* **2006**, *45*, 4642.
(11) Yoshikawa, N.; Yamabe, S.; Kanehisa, N.; Kai, Y.; Takashima, H.; Tsukahara, K. *Inorg. Chim. Acta* **2006**, *359*, 4585.
(12) Wada, T.; Yamanaka, M.; Fujihara, T.; Miyazato, Y.; Tanaka, K. *Inorg. Chem.* **2006**, *45*, 8887.
(13) Kohle, O.; Ruile, S.; Grätzel, M. *Inorg. Chem.* **1996**, *35*, 4779.
(14) Nazeeruddin, M. K.; Muller, E.; Humphry-Baker, R.; Vlachopoulos, N.; Grätzel, M. *J. Chem. Soc., Dalton Trans.* **1997**, *23*, 4571.
(15) Nazeeruddin, M. K.; Zakeeruddin, S. M.; Humphry-Baker, R.; Jirousek, M.; Liska, P.; Vlachopoulos, N.; Shklover, V.; Fischer, C. H.; Grtzel, M. *Inorg. Chem.* **1999**, *38*, 6298.
(16) Zakeeruddin, S. M.; Nazeeruddin, M. K.; Pechy, P.; Rotzinger, F. P.; Humphry-Baker, R.; Kalyanasundaram, K.; Grätzel, M.; Shklover, V.; Haibach, T. *Inorg. Chem.* **1997**, *36*, 5937.
(17) Ruile, S.; Kohle, O.; Péchy, P.; Grätzel, M. *Inorg. Chim. Acta* **1997**, *261*, 129.
(18) Klein, C.; Nazeeruddin, M. K.; Liska, P.; Censo, D. D.; Hirata, N.; Palomares, E.; Durrant, J. R.; Grätzel, M. *Inorg. Chem.* **2005**, *44*, 178.
(19) Nazeeruddin, M. K.; Péchy, P.; Grätzel, M. *Chem. Commum.* **1997**, 1705.
(20) Zubavichus, Y. V.; Slovokhotov, Y. L.; Nazeeruddin, M. K.; Zakeeruddin, S. M.; Grätzel, M.; Shklover, V. *Chem. Mater.* **2002**, *14*, 3556.
(21) Shklover, V.; Nazeeruddin, M. K.; Grätzel, M.; Ovchinnikov, Y. E. *Appl. Organomet. Chem.* **2002**, *16*, 635.
(22) Aiga, F.; Tada, T. *J. Mol. Struct.* **2003**, *658*, 25.
(23) Ghosh, S.; Chaitanya, G. K.; Bhanuprakash, K.; Nazeeruddin, M. K.; Grätzel, M.; Reddy, P. Y. *Inorg. Chem.* **2006**, *45*, 7600.

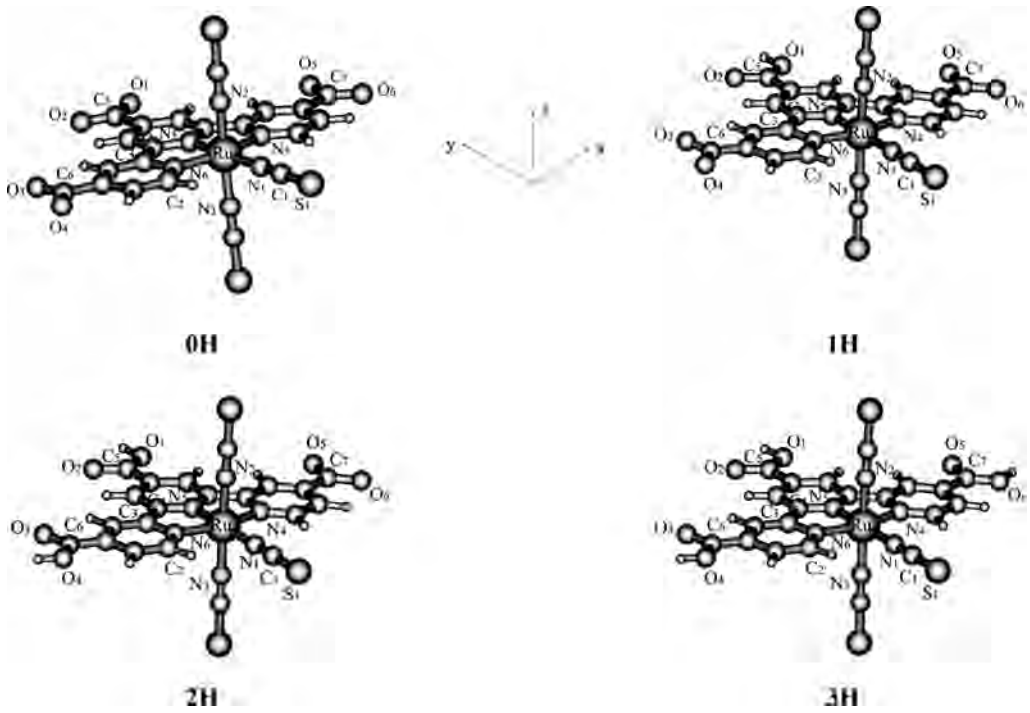

Figure 1. Optimized geometry structures of **0H**−**3H** in the ground state by DFT(B3LYP) calculations.

2. Computational Details and Theory

In this work, the C_{2v} symmetry is adopted to settle the conformation of **0H**, whereas C_S symmetry is adopted for **1H**, **2H**, and **3H**, in both ground and excited states. The geometry structures of the ground states are fully optimized using DFT with the B3LYP functional (Becke's three parameter functional and the Lee-Yang-Parr functional), [24] and the geometry structures of the excited states are fully optimized by the single-excitation configuration interaction (CIS) method.[25,26] On the basis of such calculations, spectroscopic properties related to absorption and emission are obtained by time-dependent density functional theory (TDDFT).[27] The conductor-like polarizable continuum model (CPCM)[28] is employed to account for the solvent effects of water and ethanol solvent molecules.

It is well-known that for excited states, the CIS approach is just equivalent to the HF treatment to the ground state. However, using analytic gradients and including the electronic correlation effects, the bond lengths, frequencies and dipole moments obtained at the CIS level are well in line with the experimental values.[25] Though the reasonable excited-state geometry structure can be obtained by the CIS method, the predicted transition energies usually deviate from experimental values about 1 eV or more. In recent year, TDDFT methods have been successfully used to calculate the singlet–singlet and singlet–triplet transitions in many reports.[29] More electronic correlations are involved in the TDDFT(B3LYP) approach, which then yields more accurate excitation energies than the CIS method. Therefore, on the basis of optimized geometry structures for the ground state at the DFT level and for excited states at the CIS level, we employed the TDDFT method to calculate the absorptions and emissions, respectively.

In the calculations, quasi-relativistic pseudopotentials of the Ru and S atoms proposed by Hayand Wadt[30] with 16 and 6 valence electrons, respectively, were employed, and the LanL2DZ basis sets associated with the pseudopotential were adopted. Here, the basis sets were taken as Ru (8s7p6d/6s5p3d), S (3s3p1d/2s2p1d), N (10s5p/3s2p), C (10s5p/3s2p), and H (4s/2s). Thus, 359 basis functions and 262 electrons for **0H**, 361 basis functions and 262 electrons for **1H**, 363 basis functions and 262 electrons for **2H**, and 365 basis functions and 262 electrons for **3H** were included in the calculation. All calculations were accomplished by using the Gaussian (Revision B.03) program package[31] on an Origin/3900 server.

3. Results and Discussion

3.1. Geometry Structures of 0H−3H in the Ground States. The full DFT optimizations on **0H**−**3H** indicate that the complex **0H** has a $^1A_1$ ground-state and complexes **1H**−**3H** all have $^1A'$ ground states. Their geometry structures are depicted in Figure 1, and the main optimized geometry parameters in the gas phase are listed in Table 1 together with the X-ray crystal structure data[21] of $(NBu_4^+)_2[Ru(H_2tcterpy)(NCS)_3]^{2-}$. As shown in Figure 1, the four

(24) Becke, A. D. *J. Chem. Phys.* **1993**, *98*, 5648.
(25) (a) Stanton, J. F.; Gauss, J.; Ishikawa, N.; Head-Gordon, M. *J. Chem. Phys.* **1995**, *103*, 4160. (b) Foreman, J. B.; Head-Gordon, M.; Pople, A. *J. Phys. Chem.* **1992**, *96*, 135. (c) Waiters, V. A.; Hadad, C. M.; Thiel, Y.; Colson, S. D.; Wibergy, K. B.; Johnson, P. M.; Foresmanl, J. B. *J. Am. Chem. Soc.* **1991**, *113*, 4782.
(26) (a) Zhang, H. X.; Che, C. M. *Chem. Eur. J.* **2001**, *7*, 4887. (b) Pan, Q. J.; Zhang, H. X. *J. Chem. Phys.* **2003**, *119*, 4346. (c) Pan, Q. J.; Zhang, H. X. *J. Phys. Chem. A* **2004**, *108*, 3650. (d) Pan, Q. J.; Zhang, H. X. *Eur. J. Inorg. Chem.* **2003**, 4202. (e) Pan, Q. J.; Zhang, H. X. *Inorg. Chem.* **2004**, *43*, 593. (f) Liu, T.; Zhang, H. X.; Shu, X.; Xia, B. H. *Dalton Trans.* **2007**, 1922. (g) Liu, T.; Xia, B. H.; Zhou, X.; Zhang, H. X.; Pan, Q. J.; Gao, J. S. *Organometallics* **2007**, *26*, 143. (h) Liu, T.; Gao, J. S.; Xia, B. H.; Zhou, X.; Zhang, H. X. *Polymer* **2007**, *48*, 502.
(27) (a) Casida, M. E.; Jamorski, C.; Casida, K. C.; Salahub, D. R. *J. Chem. Phys.* **1998**, *108*, 4439. (b) Stratmann, R. E.; Scuseria, G. E. *J. Chem. Phys.* **1998**, *109*, 8218. (c) Matsuzawa, N. N.; Ishitani, A. *J. Phys. Chem. A* **2001**, *105*, 4953.
(28) (a) Barone, V.; Cossi, M. *J. Phys. Chem. A* **1998**, *102*, 1995. (b) Cossi, M.; Rega, N.; Scalmani, G.; Barone, V. *J. Comput. Chem.* **2003**, *24*, 669.
(29) (a) Bauernschmitt, R.; Ahlrichs, R. *Chem. Phys. Lett.* **1996**, *256*, 454. (b) Rosa, A.; Baerends, E. J.; Gisbergen, S. J. A. V.; Lenthe, E. J.; Groeneveld, A.; Snijders, J. G. *J. Am. Chem. Soc.* **1999**, *121*, 10356.
(30) (a) Wadt, W. R.; Hay, P. J. *J. Chem. Phys.* **1985**, *82*, 284. (b) Hay, P. J.; Wadt, W. R. *J. Chem. Phys.* **1985**, *82*, 299.

Table 1. Partial Optimized Geometry Structural Parameters of **0H**−**3H** in the Ground and the Lowest Triplet Excited States Using DFT and CIS Methods, Respectively, Together with Experimental Data for $(NBu_4^+)_2[Ru(H_2tcterpy)(NCS)_3]^{2-}$

	0H		**1H**		**2H**		**3H**		
parameters	$^1A_1$	$^3A_1$	$^1A'$	$^3A'$	$^1A'$	$^3A'$	$^1A'$	$^3A'$	exptl[a]
				Bond Lengths (Å)					
Ru−N1	2.139	2.208	2.107	2.146	2.088	2.133	2.073	2.412	2.052
Ru−N2	2.074	2.165	2.057	2.099	2.047	2.106	2.040	2.240	2.032
Ru−N3	2.074	2.165	2.057	2.098	2.047	2.106	2.040	2.240	
Ru−N4	2.097	2.183	2.099	2.175	2.074	2.148	2.062	2.220	
Ru−N5	1.974	2.042	1.938	1.994	1.941	1.991	1.937	2.232	1.936
Ru−N6	2.097	2.183	2.099	2.175	2.074	2.148	2.062	2.220	2.090
N1−C1	1.190	1.158	1.192	1.159	1.193	1.161	1.195	1.163	
C1−S1	1.710	1.722	1.696	1.709	1.688	1.703	1.680	1.701	
N6−C2	1.357	1.353	1.357	1.340	1.358	1.340	1.358	1.328	
N6−C3	1.387	1.363	1.384	1.365	1.389	1.373	1.389	1.357	
N5−C4	1.372	1.360	1.381	1.354	1.379	1.357	1.379	1.322	
C3−C4	1.484	1.502	1.477	1.475	1.474	1.477	1.473	1.500	
C5−O1	1.292	1.267	1.407	1.370	1.396	1.358	1.396	1.353	
C5−O2	1.292	1.267	1.254	1.230	1.252	1.226	1.248	1.216	
C6−O3	1.292	1.267	1.290	1.264	1.280	1.253	1.245	1.216	
C6−O4	1.292	1.267	1.290	1.264	1.374	1.339	1.390	1.352	
C7−O5	1.292	1.267	1.290	1.264	1.280	1.253	1.245	1.216	
C7−O6	1.292	1.267	1.290	1.264	1.280	1.253	1.390	1.352	
				Bond Angles (deg)					
N6−Ru−N5	79.6	79.6	80.2	78.7	80.41	79.1	80.5	74.9	81.1
N6−Ru−N4	159.2	156.2	160.3	157.4	160.8	158.2	161.1	149.8	161.6
N2−Ru−N3	176.8	178.1	177.1	179.8	177.4	177.3	177.4	172.6	177.4
N1−Ru−N6	100.4	101.9	99.8	101.3	99.6	100.9	99.5	105.1	101.4

[a] From ref 21.

complexes show a pseudo-octahedral coordination for the RuN_6 core, because the Ru(II) atoms adopt the low-spin $4d^65s^0$ electronic configurations. Also the coordination axis is shown in Figure 1. The terpy-Ru-N1C1S1 moiety lies on the *xy* plane, and the two NCS ligands are slightly tilted with respect to the *z* axis. From Table 1, we can see that the optimized geometry structural parameters are in excellent agreement with the available X-ray data and consistent with those calculated by Aiga and co-worker[22] by PBE0 approach.[32] In a simple Dewar, Chatt, and Duncanson model,[33,34] the bond interaction can be described as a donation from a σ molecular orbital of the ligand (i.e., CN^- or SCN^-) toward an empty d orbital of metal and a concurrent back-donation from a filled (or partially filled) d orbital to a π^* antibonding orbital of the ligand. The two processes can promote and strengthen each other. Because polypyridine ligands have σ-donating orbitals localized on N and π-donating and π^*-accepting orbitals delocalized on aromatic rings, back-donation between Ru and the π^* orbitals is significant.[35] In the four complexes the calculated Ru−N5 bond lengths are shorter than the Ru−N4,6 by ca. 0.12–0.16 Å, whereas the Ru−N1 bond lengths are longer than the Ru−N2,3 bond lengths by ca. 0.03–0.07 Å. The reason is that the central pyridine is *trans* to the stronger electron-donating anionic NCS ligand compared to the two peripheral pyridine rings, which are less σ-donating compared to the NCS ligand. It is noted that the bond distances of N−C within the terpyridine rings are about 1.35–1.38 Å, ca. 0.1 Å shorter than a normal N−C single bond, indicating that there are some delocalizations of the lone pairs of the nitrogen atoms.

It is interesting to notice that the Ru−N distances are shortened about 0.01–0.04 Å for each step of protonation. For the fully protonated form (**3H**), the Ru−N1, Ru−N2,3, Ru−N4,6, and Ru−N5 bond lengths are 2.073, 2.040, 2.062, and 1.937 Å, respectively; these parameters shift to, respectively, 2.139, 2.074, 2.097, and 1.974 Å in the full deprotonated form (**0H**), probably as a result of the decreased π back-donation from the metal Ru to the terpyridines π^* orbitals associated with the energy raise of the terpyridine-based LUMOs (see below). In addition to the bond length, the main bond angles are accurately reproduced.

3.2. Absorption Spectra. 3.2.1. Electronic Structures. It will be useful to examine the nature of the frontier molecular orbitals for these Ru(II) complexes to provide the framework for the excited-state TDDFT and CIS calculations in the subsequent section. Moreover, the frontier molecular orbitals play a relevant role in such systems, because they

(31) *Gaussian 03*, Revision B.03; Frisch, M. J.; Trucks, G. W.; Schlegel, H. B.; Scuseria, G. E.; Robb, M. A.; Cheeseman, J. R.; Montgomery, J. A.; Vreven, Jr., T.; Kudin, K. N.; Burant, J. C.; Millam, J. M.; Iyengar, S. S.; Tomasi, J.; Barone, V.; Mennucci, B.; Cossi, M.; Scalmani, G.; Rega, N.; Petersson, G. A.; Nakatsuji, H.; Hada, M.; Ehara, M.; Toyota, K.; Fukuda, R.; Hasegawa, J.; Ishida, M.; Nakajima, T.; Honda, Y.; Kitao, O.; Nakai, H.; Klene, M.; Li, X.; Knox, J. E.; Hratchian, H. P.; Cross, J. B.; Adamo, C.; Jaramillo, J.; Gomperts, R.; Stratmann, R. E.; Yazyev, O.; Austin, A. J.; Cammi, R.; Pomelli, C.; Ochterski, J. W.; Ayala, P. Y.; Morokuma, K.; Voth, G. A.; Salvador, P.; Dannenberg, J. J.; Zakrzewski, V. G.; Dapprich, S.; Daniels, A. D.; Strain, M. C.; Farkas, O.; Malick, D. K.; Rabuck, A. D.; Raghavachari, K.; Foresman, J. B.; Ortiz, J. V.; Cui, Q.; Baboul, A. G.; Clifford, S.; Cioslowski, J.; Stefanov, B. B.; Liu, G.; Liashenko, A.; Piskorz, P.; Komaromi, I.; Martin, R. L.; Fox, D. J.; Keith, T.; Al-Laham, M. A.; Peng, C. Y.; Nanayakkara, A.; Challacombe, M.; Gill,P. M. W.; Johnson, B.; Chen, W.; Wong, M. W.; Gonzalez, C.; Pople, J. A. Gaussian, Inc.: Pittsburgh, PA, 2003.
(32) Adamo, C.; Scuseria, G. E.; Barone, V. *J. Chem. Phys.* **1999**, *111*, 2889.
(33) Dewar, M. J. S. *Bull. Soc. Chim. Fr.* **1951**, *18*, C71.
(34) Chatt, J.; Duncanson, L. A. *J. Chem. Soc.* **1953**, 2939.
(35) Boulet, P.; Chermette, H.; Daul, C.; Gilardoni, F.; Rogemond, F.; Weber, J.; Zuber, G. *J. Phys. Chem. A* **2001**, *105*, 885.

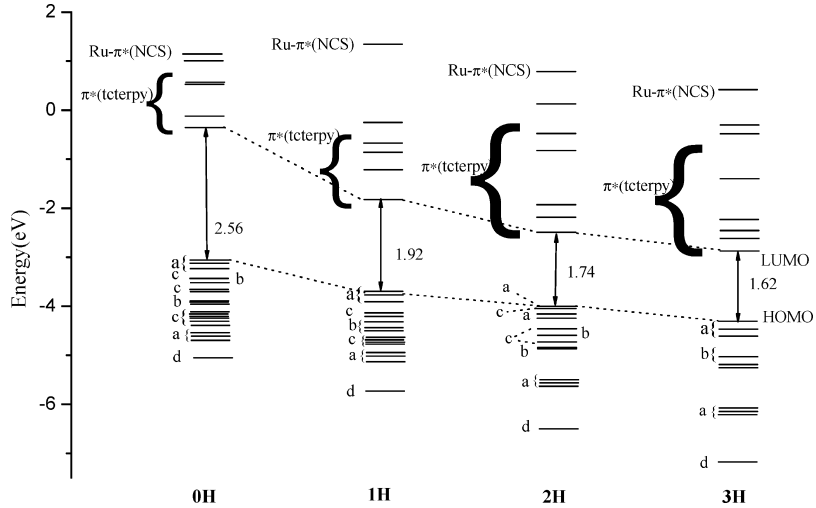

Figure 2. Plot of the frontier molecular orbitals relevant to the absorptions for **0H**−**3H** in ethanol solution, calculated by the TDDFT method.

Table 2. Partial Molecular Orbital Compositions (%) of **0H** in Ethanol by TDDFT Calculations

		composition (%)				Ru components(%)			
MO	energy (eV)	Ru	terpy	COO^-	NCS	s	p	d	assignment of orbital
$59a_1$	1.1816	49.0	22.9	0.6	27.5	7.4s	$15.6p_y$	$25.7d_{x^2-y^2}$	$s/p_y/d_{x^2-y^2}$(Ru)-π*(NCS)
$23b_1$	1.1755	1.3	90.7	7.9	0.1				π*(tcterpy)
$12a_2$	0.5181	3.4	89.3	7.2	0.1			$3.4d_{xz}$	π*(tcterpy)
$22b_1$	0.4909	0.8	91.4	7.6	0.2				π*(tcterpy)
$11a_2$	−0.2204	2.5	96.0	1.4	0.2			$2.5d_{xz}$	π*(tcterpy)
$21b_1$(L)	−0.4637	7.7	86.1	4.2	3.1			$7.6d_{yz}$	π*(tcterpy)
				HOMO–LUMO Energy Gap					
$20b_1$(H)	−3.0270	46.7	11.3	0.7	41.3			$46.2d_{yz}$	d_{yz} (Ru)-π*(NCS)
$10a_2$	−3.0665	50.1	7.7	0.5	41.5			$50.1d_{xz}$	d_{xz} (Ru)-π*(NCS)
$43b_2$	−3.2798	49.6	16.6	0.5	33.2			49.2_{xy}	d_{xy} (Ru)-π*(NCS)
$42b_2$	−3.7473	0.0	18.6	81.2	0.1				$p_x/p_y(COO^-)$
$19b_1$	−3.7636	0.3	0.5	0.0	99.3				Π*(NCS)
$41b_2$	−3.7808	0.0	16.7	82.7	0.7				$p_x/p_y(COO^-)$
$58a_1$	−3.7813	0.1	16.9	83.0	0.0				$p_x/p_y(COO^-)$
$40b_2$	−3.8777	0.3	4.1	0.3	95.3				Π*(NCS)
$57a_1$	−3.8896	0.1	1.7	0.0	98.2				Π*(NCS)
$9a_2$	−4.0548	0.1	3.5	95.8	0.6				$p_z(COO^-)$
$8a_2$	−4.0956	0.0	1.5	98.5	0.0				$p_z(COO^-)$
$7a_2$	−4.3541	31.7	16.8	2.3	49.2			$31.7d_{xz}$	d_{xz} (Ru)-π*(NCS)
$6a_2$	−5.0712	2.5	94.5	1.7	1.2			$2.5d_{xz}$	π(tcterpy)

rule the electronic excitations and the transition character. The frontier molecular orbitals are plotted according to their energies in Figure 2 for complexes **0H**−**3H** to illuminate the effect of the protonation. The frontier molecular orbital compositions of **0H** in ethanol are compiled in Table 2, and those of **1H**−**3H** are shown in Table S1 (see Supporting Information). We display the electron density diagrams of the partial important frontier molecular orbitals for complex **0H** in ethanol in Figure 3.

For all of the considered complexes, the pattern of the occupied molecular orbitals is qualitatively similar. As depicted in Figure 2, the higher energy occupied molecular orbitals can be classified as four types, which are labeled as a, b, c, and d, respectively. The a type has essentially ruthenium d character with a sizable contribution coming from the NCS ligand orbitals, mixed in an antibonding fashion with a metal atom. The b type is a set of pure NCS π orbitals. This significant thiocyanate character in the HOMOs was already found in the N3 dye[36,37] and seems to play an important role in the regeneration of dye-sensitized solar cells.[37] The c type is mainly localized on the COO^- ligands with little metal character. The d type is combined π banding orbitals localized on the terpyridine ligands. In complexes **0H**, **1H**, and **3H**, HOMO, HOMO-1, and HOMO-2 are antibonding combinations of the Ru d orbitals with the NCS π orbitals, whereas in complex **2H**, one oxygen lone pair type orbital (HOMO-1) inserts into the three Ru(d)-NCS MOs. It is interesting to note that, in the Ru(d)-NCS character HOMOs, the contributions of ruthenium d orbitals are decreased from **0H** to **3H** (see Table 2 and Table S1). This kind of decrease is reasonable given that the electron-withdrawing ability of the COOH groups is stronger than that of the COO^- groups.

The five lower-energy unoccupied molecular orbitals of the investigated complexes are π* orbitals localized on the pyridine ligands, with considerable contribution arising from the carboxylic groups. In photovoltaic solar cells the carboxylic units serve as anchoring groups to the TiO_2 semicon-

(36) Monat, J. E.; Rodriguez, J. H.; McCusker, J. K. *J. Phys. Chem. A* **2002**, *106*, 7399.
(37) Fantacci, S.; Angelis, F. D.; Selloni, A. *J. Am. Chem. Soc.* **2003**, *125*, 4381.

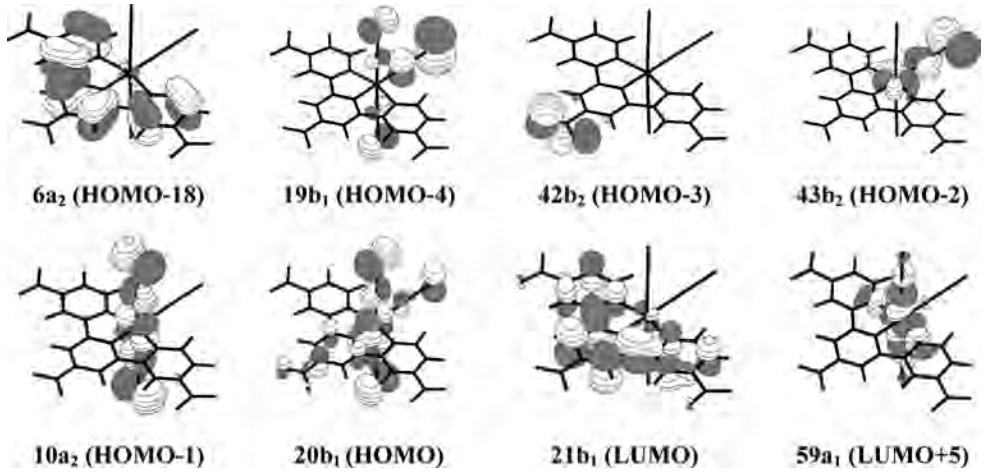

Figure 3. Electron density diagrams of the frontier molecular orbitals relevant to the absportions of **0H** in ethanol by TDDFT calculations.

ductor surface. Therefore, such a contribution from the carboxylic groups to the π^* LUMOs, which represent the final states in MLCT transitions (see below), should favor the electron-injection process from the dye excited state to the semiconductor surface.[2,3] This is due to the electron-withdrawing character of the terminal carboxylic groups, which lower the energies of the π^* LUMOs, thus increasing electronic coupling between the donating orbital of the excited dye and the conduction band of the acceptor TiO_2.

Comparison of the molecular orbital energy levels for the various protonated complexes (**0H**−**3H**) in ethanol solution shows that protonation of the terminal COOH group results in a larger stabilization of the occupied and unoccupied orbitals localized on the terpyridine and COO^- moieties. For each step of protonation, the stabilization of the unoccupied orbitals is more dramatic with respect to the occupied orbitals. Thus, the HOMO–LUMO energy gaps decreases from 2.56 to 1.62 eV (the HOMO–LUMO energy gaps of complexes **0H**, **1H**, **2H**, and **3H** are 2.56, 1.92, 1.74, and 1.62 eV, respectively) as a result of the stabilization of the unoccupied terpyridine π^* orbitals due to the increased electron density on the protonated carboxylic groups. A similar effect has been found in N3 and N3-derived dyes.[8,10,38]

3.2.2. Absorption Spectra in Ethanol. We obtained the absorption spectra of **0H**−**3H** in the ethanol solution by TDDFT(B3LYP) with CPCM calculations. The calculated absorptions associated with their oscillator strengths, main configurations, and the assignments as well as the experimental results are summarized in Table 3. The fitted Gaussian-type absorption curves with the calculated absorption data together with the experimental absorption spectra are shown in Figure 4.

With respect to **0H**, the lowest-energy absorption in ethanol is calculated at 575 nm, which originates from the $X^1A_1 \rightarrow A^1B_2$ transition, has an oscillator strength of 0.0411, and is comparable to the experimental 590 nm absorption.[6] In the excitation, the $20b_1$(HOMO) $\rightarrow 11a_2$(LUMO + 1) configuration has the largest coefficient (about 0.69) in CI wave functions, which is responsible for the absorption. As shown in Table 2, the $20b_1$ (HOMO) orbital is formed by 46% d_{yz}(Ru) and 41% NCS π orbitals, whereas the $11a_2$(LUMO + 1) orbital is π^* orbitals delocalized over the whole tcterpy ring. Therefore, the absorption at 575 nm can be assigned as the combination of d_{yz}(Ru)$\rightarrow\pi^*$(tcterpy) charge transfer (MLCT) and NCS$\rightarrow\pi^*$(tcterpy) (ligand to ligand charge transfer, LLCT) transitions. The B^1A_1 and C^1B_2 excited states of **0H** arise from the absorptions at 538 and 419 nm, which are comparable to the experimental 528 and 400 nm absorptions,[6] respectively. As shown in Tables 2 and 3, the 538 and 419 nm transitions are unambiguously attributed to the admixture of d_{yz} and/or d_{xz}(Ru)$\rightarrow\pi^*$(tcterpy) (MLCT) and NCS$\rightarrow\pi^*$(tcterpy) (LLCT) transitions. So the lower-energy absorptions of **0H** are dominated by MLCT and LLCT transitions.

As shown in Table 3, in the lower-energy region at $\lambda >$ 400 nm of the absorption spectra, the protonated complexes at different degree (**1H**, **2H**, and **3H**) show transition characteristics similar to that discussed above for the full deprotonated complex (**0H**). The calculated lowest-energy MLCT/LLCT absorptions for complexes **0H**−**3H** are at 575, 617, 770, and 862 nm, respectively. The red shifts of this lower-energy absorption band going from the fully deprotonated to the fully protonated form are mainly due to the stronger electron-withdrawing nature of the carboxylic acid groups compared to the carboxylate anions on the terpyridine ligand. Furthermore, to understand the energy shift of the MLCT/LLCT transitions when the terpyridine ligand is functionalized by the carboxylic acid groups, it is crucial to examine how the low-lying unoccupied terpy orbitals are affected by these anchoring groups. For the carboxylic acid substituted terpyridine ligand, the inductive effect of the anchoring group leads to a strong electron density delocalization in the π^* LUMO. Moreover, the protons in the carboxylic group take electron density from this group, increasing the inductive effect of the substituent on the terpyridine ligand. As a result, the energy level of the unoccupied terpyridine π^* orbital decreases and the MLCT/

(38) Angelis, F. D.; Fantacci, S.; Selloni, A. *Chem. Phys. Lett.* **2004**, *389*, 204.

Table 3. Calculated Absorptions of **0H**−**3H** in Ethanol at the TDDFT(B3LYP) Level, Together with Experimental Values

	states	config (CI coeff)	E_{nm}(eV)	oscillator strength	assignment	exptl (nm)[a]
0H	A^1B_2	$20b_1 \rightarrow 11a_2$ (0.69)	575 (2.16)	0.0411	MLCT/LLCT	590
	B^1A_1	$10a_2 \rightarrow 11a_2$ (0.61)	538 (2.31)	0.0407	MLCT/LLCT	528
		$20b_1 \rightarrow 21b_1$ (0.26)			MLCT/LLCT	
	C^1B_2	$10a_2 \rightarrow 22b_1$ (0.68)	419 (2.96)	0.0875	MLCT/LLCT	400
	D^1A_1	$9a_2 \rightarrow 11a_2$ (0.67)	382 (3.25)	0.0185	LLCT	
	E^1B_2	$6a_2 \rightarrow 21b_1$ (0.57)	309 (4.01)	0.2676	$\pi \rightarrow \pi^*$	338, 326
		$7a_2 \rightarrow 22b_1$ (0.20)			MLCT/LLCT	
	F^1B_2	$43b_2 \rightarrow 59a_1$ (0.72)	303 (4.09)	0.0273	MC/LLCT	
	G^1B_2	$8a_2 \rightarrow 22b_1$ (0.21)	301 (4.12)	0.0212	LLCT	
		$9a_2 \rightarrow 22b_1$ (0.62)			LLCT	
1H	A^1A'	$29a'' \rightarrow 32a''$ (0.69)	617 (2.01)	0.0268	MLCT/LLCT	
	B^1A'	$28a'' \rightarrow 31a''$ (0.48)	592 (2.09)	0.1300	LLCT/LMCT	610
		$30a'' \rightarrow 32a''$ (0.42)			MLCT/LLCT	
	C^1A''	$97a' \rightarrow 31a''$ (0.70)	591 (2.10)	0.0443	LLCT/LMCT	
	D^1A'	$25a'' \rightarrow 31a''$ (0.58)	496 (2.50)	0.0221	MLCT/LLCT	542
		$30a'' \rightarrow 33a''$ (0.40)			MLCT/LLCT	
	E^1A'	$24a'' \rightarrow 31a''$ (0.50)	417 (2.98)	0.0228	MLCT/LLCT	413
		$30a'' \rightarrow 34a''$ (0.42)			MLCT/LLCT	
	F^1A'	$26a'' \rightarrow 33a''$ (0.66)	357 (3.47)	0.0164	LLCT	
	G^1A'	$23a'' \rightarrow 31a''$ (0.46)	343 (3.61)	0.1536	$\pi \rightarrow \pi^*$	339, 328
		$24a'' \rightarrow 32a''$ (0.47)			MLCT/LLCT	
	H^1A'	$94a' \rightarrow 102a'$ (0.22)	325 (3.81)	0.0248	MC/LLCT	
		$101a' \rightarrow 102a'$ (0.41)			MC/LLCT	
	I^1A'	$25a'' \rightarrow 33a''$ (0.53)	318 (3.91)	0.1283	MLCT/LLCT	
		$26a'' \rightarrow 34a''$ (0.32)			LLCT	
2H	A^1A'	$29a'' \rightarrow 32a''$ (0.63)	770 (1.61)	0.0623	MLCT/LLCT	
	B^1A'	$27a'' \rightarrow 31a''$ (0.46)	699 (1.77)	0.1064	LLCT/LMCT	
		$29a'' \rightarrow 33a''$ (0.21)			MLCT/LLCT	
	C^1A''	$97a' \rightarrow 31a''$ (0.68)	674 (1.84)	0.0451	LLCT/LMCT	
	D^1A'	$29a'' \rightarrow 33a''$ (0.61)	645 (1.92)	0.0369	MLCT/LLCT	620
		$30a'' \rightarrow 33a''$ (0.22)			MLCT/LLCT	
	E^1A'	$26a'' \rightarrow 31a''$ (0.49)	510 (2.43)	0.0213	MLCT/LLCT	542
		$27a'' \rightarrow 33a''$ (0.45)			LLCT	
	F^1A'	$25a'' \rightarrow 32a''$ (0.41)	413 (3.00)	0.0751	MLCT/LLCT	413
		$26a'' \rightarrow 32a''$ (0.45)			MLCT/LLCT	
	G^1A'	$28a'' \rightarrow 35a''$ (0.68)	353 (3.51)	0.0266	LLCT	
	H^1A'	$24a'' \rightarrow 31a''$ (0.60)	347 (3.58)	0.2341	$\pi \rightarrow \pi^*$	342, 329
		$25a'' \rightarrow 33a''$ (0.27)			MLCT/LLCT	
3H	A^1A'	$30a'' \rightarrow 32a''$ (065)	862 (1.44)	0.0426	MLCT/LLCT	
	B^1A'	$29a'' \rightarrow 33a''$ (0.65)	754 (1.64)	0.0781	MLCT/LLCT	
	C^1A'	$29a'' \rightarrow 32a''$ (0.20)	689 (1.80)	0.1218	MLCT/LLCT	625
		$30a'' \rightarrow 33a''$ (0.57)			MLCT/LLCT	
	D^1A'	$28a'' \rightarrow 33a''$ (0.68)	597 (2.08)	0.0622	LLCT	
	E^1A'	$27a'' \rightarrow 31a''$ (0.66)	513 (2.42)	0.0529	MLCT/LLCT	556
	F^1A'	$26a'' \rightarrow 32a''$ (0.68)	416 (2.98)	0.0199	MLCT/LLCT	429
	G^1A'	$25a'' \rightarrow 31a''$ (0.64)	334 (3.71)	0.2745	$\pi \rightarrow \pi^*$	344, 330
	H^1A'	$98a' \rightarrow 102a'$ (0.26)	318 (3.90)	0.0320	MC/LLCT	
		$101a' \rightarrow 102a'$ (0.47)				

[a] from ref 6.

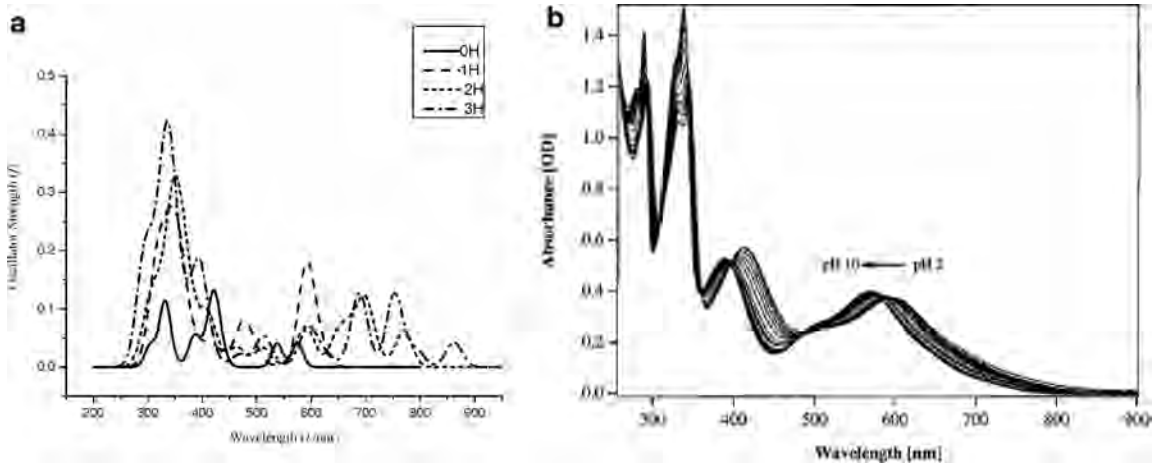

Figure 4. (a) Simulated absorption spectra of **0H**−**3H** in ethanol. (b) Experimental absorption spectral changes of the black dye as a function of pH.

LLCT band is red-shifted by the introduction of protons onto carboxylate anions groups.

Complexes **0H**−**3H** have broad absorptions in the visible region and extending to the near-IR region, which mostly

owe to two factors. First, the tcterpyridine ligands have the low-lying π^* molecular orbital; second, the strong donor NCS ligands can destabilized the metal Ru t_{2g} orbital. Thus, the transition energy decreases, and absorption band is red-shifted.

In the lower-energy region, what is particular with respect to the full deprotonated species (**0H**) is that the various protonated forms (**1H**−**3H**) have the moderate intense absorptions with the LLCT/LMCT character. In complex **1H**, one LLCT/LMCT type transition at 591 nm, which mainly arises from the 97a′→31a″ (0.70) configurations, is described as NCS→π^*(tcterpy) and NCS→d_{yz}(Ru) transitions. Compared with **1H**, the LLCT/LMCT absorptions of **2H** at 699 and 674 nm are more intense. In addition, there is an pure LLCT absorption at 597 nm for **3H** and the excitation of 28a″→33a″ (CI = 0.68) corresponds to the transition and can be assigned to the NCS→π^*(tcterpy) transition. It is worth noting that the lower-energy absorptions display the decreasing MLCT character and the increasing LLCT character from complexes **0H** to **3H**. This trend of the transition nature is reasonable given that the composition of ruthenium in the HOMOs is decreasing from **0H** to **3H**, whereas the contribution of thiocyanate orbitals is increasing from **0H** to **3H**. Thus, the lower-energy absorptions for the complexes **1H**−**3H** can be regarded as the measured absorptions in the visible region, which have the MLCT and/or LLCT character and involve a small LMCT component.

We now look at the higher-energy absorptions in the complexes. It has been found that the calculated electronic absorptions for the complexes **0H**−**3H** at 309, 343, 347, and 334 nm with the largest oscillator strength of 0.2676, 0.1536, 0.2341, and 0.2745, respectively, are more suggestive to be most likely observed in the experiment. These absorptions have intraligand $\pi\rightarrow\pi^*$ transition character (see Table 3) and are attributed to the π(tcterpy)→π^*(tcterpy) transition. However, this kind of transition is perturbed by the combined MLCT/LLCT components. Indeed, the participation of the MLCT/LLCT components in the UV–visible region absorption is usual and even more remarkable in the lower-energy absorption bands.

In the calculations, the MC (metal-centered) transition absorptions for **0H**, **1H**, and **3H** in ethanol are obtained at 303, 325, and 318 nm, respectively. With respect to **0H**, the 303 nm transition mainly derives from the excitation of $43b_2$→$59a_1$ (0.72) configuration as seen Table 3. As shown in Table 2 and Figure 3, the $43b_2$ orbital has 49% Ru(d_{xy}) and 33% NCS ligand that lies on the *xy* plane, while the $59a_1$ orbital is mainly located upon the Ru(s)(7%), Ru(p_y)(16%), Ru(d_z^2)(26%), and NCS ligands (28%), which are slightly tilted with respect to the *z* axis. So we attribute the 303 nm absorption of **0H** to MC/LLCT transition. Similar to **0H**, the 325 and 318 nm absorptions of complexes **1H** and **3H**, respectively, can be regarded as MC/LLCT transitions.

The other higher-energy absorptions in the UV–visible region have the LLCT character, which are calculated at 382 and 301 nm for **0H**, 357 and 318 nm for **1H**, and 353 nm for **2H**. Table 2 shows that the occupied orbitals $8a_2$ and $9a_2$ of **0H**, the 26a″ orbital of **1H**, and the 28a″ orbital of **2H** all localized on the carboxylate anion groups and concentrated on the O(p_z) orbital. However, the unoccupied orbitals $11a_2$ and $22b_1$ of **0H**, the 33a″ and 34a″ orbitals of **1H**, and 35a″ orbital of **2H** are a set of tcterpyridine π^* orbitals. Thus, this type of absorption for complexes **0H**, **1H**, and **2H** can be regarded as O(p_z)→π^*(tcterpy) (LLCT) transitions. Because the fully protonated complex (**3H**) has no carboxylate anion groups, no O(p_z)→π^*(tcterpy) (LLCT)) transitions are observed in its absorptions.

A comparison between the experimental and theoretical absorption spectra of black dye in ethanol solution is reported in Figure 4. In experiments, the 800–400 nm regions have been assigned as the Ru to tcterpy ligand charge transfer bands, and the 400–300 nm absorptions are attributed to the $\pi\rightarrow\pi^*$ charge transfer transitions.[6] We notice that the agreement between theory and experiment is good in terms of both band positions and relative intensity. The 400–800 nm absorption bands have less intensity than the 300–400 nm absorption bands. However, there are some differences between the theory calculation and the experimental investigation. As mentioned above, we assign the lower-energy absorptions of **0H**−**3H** as mixed Ru-NCS to tcterpyridine charge transfer (MLCT/LLCT) rather than to pure metal-ligand charge transfer (MLCT) transitions, originating from a set of Ru-NCS d-π^* orbitals, while the highest energy absorptions of **0H**−**3H** from intraligand tcterpyridine $\pi\rightarrow\pi^*$ charge transfer (ILCT) are involved in a sizable strength O(p_z)→terpy charge transfer (LLCT) transitions. Apparently, the calculated absorptions of **0H**−**3H** reflect the experimental observation and provide more detailed information about transition properties of the absorption.

3.2.3. Solvent Effects. To check the solvent dependence of spectroscopic properties, we also calculated the absorptions of **0H**−**3H** in the gas phase and water solution, and the results are listed in Tables S2 and S3 in Supporting Information. The frontier molecular orbital compositions of **0H**−**3H** in the gas phase and water solution are shown in Table S4 and Table S5, respectively. A comparison of the relevant molecular orbital energy level of the absorption for **0H**−**3H** in gas, ethanol, and water are presented in Figure S1. From Figure S1 and Tables S4 and S5, we can see that the solvent effect leads to a sizable change of both energies and composition of the molecular orbitals. The LUMOs of **0H**−**3H** all maintain similar compositions in terms of terpyridine and carboxylic group contributions in gas phase and ethanol. On the other hand, in ethanol, the HOMOs for **0H** and **1H** show similar contribution of ruthenium d orbitals mixed with NCS ligand orbitals. The HOMO of **2H** in ethanol solution shows a high composition of ruthenium *d* orbitals (30%) mixed with NCS ligand orbitals (58%), whereas in the gas phase, the HOMO is centered on the oxygen lone pairs of the carboxylate group. For **3H**, the HOMO in ethanol has similar character as in the gas phase but has a somewhat different composition in terms of atomic orbitals, with slightly larger percentages of metal states. In the complexes **1H**−**3H**, the HOMO is more stabilized than

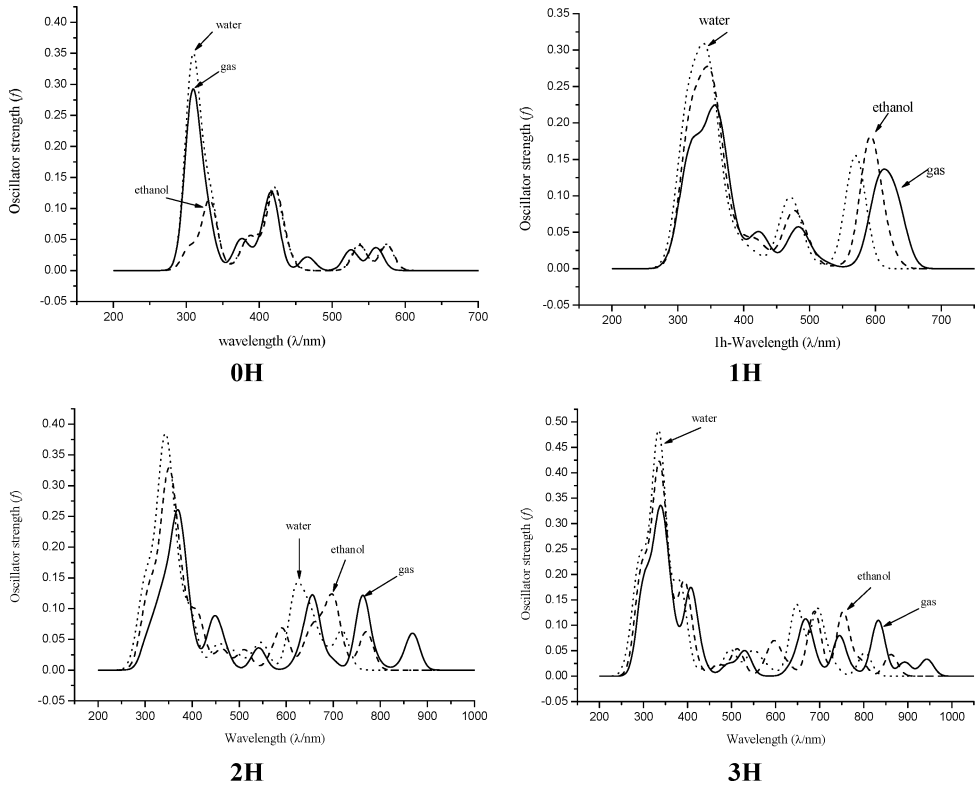

Figure 5. Simulated absorption spectra of **0H**−**3H** in the gas phase and ethanol and water solutions.

the LUMO, whereas in **0H** the LUMO is more stabilized than the HOMO. In ethanol, both the HOMO and LUMO of **0H** are significantly stabilized by 6.80 and 6.84 eV, respectively, with respect to the corresponding values computed in gas phase. For complex **1H** in ethanol, the HOMO is stabilized by 5.12 eV, and LUMO is stabilized by 5.00 eV. For complex **2H** in ethanol, the HOMO is stabilized by 3.76 eV, and LUMO is stabilized by 3.29 eV. For complex **3H** in ethanol, the HOMO is stabilized by 1.89 eV, and LUMO is stabilized by 1.76 eV. For **1H**−**3H** complexes, the presence of the solvent leads to a slightly increase of the HOMO–LUMO gap, which changes from 1.80, 1.26, and 1.48 eV, respectively, in the gas phase to 1.92, 1.74, and 1.62 eV, respectively, in ethanol. In contrast to the others, the HOMO–LUMO energy gap of **0H** is lowered in ethanol compared to that in the gas phase (i.e., 2.56 eV in ethanol and 2.60 eV in the gas phase). The change of HOMO–LUMO energy gap indicates that solvent effect leads the absorptions of **0H** red shift and the absorptions of **1H**−**3H** blue shift. Moreover, the electronic structures of **0H**−**3H** in water are similar to those found in ethanol and the LUMOs and HOMOs of **1H**−**3H** are further stabilized, resulting in a HOMO–LUMO gap of 2.0, 1.87, and 1.73 eV, respectively.

The fitted absorption spectra of complexes **0H**−**3H** in gas, ethanol, and water are shown in Figure 5. As listed in Table 3 and Tables S2 and S3, the CI configurations, oscillator strengths, and character of transitions calculated in the gas phase, ethanol, and water are rather similar. It is evident that the spectra in solutions are in considerably better agreement with the experiment than the spectra computed in the gas phase. In both solvents, the lower-energy absorption bands are dominated by MLCT/LLCT transitions, whereas the higher-energy absorption band with the most intensity, is attributed to the intraligand $\pi \rightarrow \pi^*$ charge transfer mixed with $O(p_z) \rightarrow$terpy charge transfer transitions. As shown in Figure 5, for the fully deprotonated form (**0H**), the lower-energy absorptions are red-shifted in ethanol and water with respect to the gas phase. On the other hand, for the protonated complexes (**1H**−**3H**), the lower-energy absorption bands are blue-shifted in ethanol and water with respect to the gas phase. As shown in Figure 5, the negative solvatochromism in the MLCT/LLCT band (λ = 400–800 nm) of **1H**−**3H** complexes is observed. With increasing solvent polarity from ethanol to water, the MLCT/LLCT absorptions are further blue-shifted. In addition, we find that the $\pi \rightarrow \pi^*$ band is slightly affected by the solvent polarity. These conclusions are in excellent agreement with the experimental facts. There is a factor that can be responsible for the observed blue-shift from ethanol to water: the electrostatic effect between water solvent and NCS ligand is stronger than that between ethanol solvent and NCS ligand.

To gain insight into the origin of solvent effect of the MLCT/LLCT absorptions, it is useful to keep in mind the dipole moments of complexes. As discussed above, the MLCT/LLCT transitions involve displacement of charge from Ru center and the NCS ligand toward the tcterpyridine π^* orbitals. Thus, to approximately evaluate the dipole moment in the excited states, we considered the electronic state in which one electron is promoted from the HOMO to the LUMO. The excited-state dipole moments in the gas phase, ethanol, and water are predicted at the B3LYP/LAN2DZ level on the basis of the optimized ground-state geometry. Table S6 gives the dipole moments of the complexes **0H**−**3H** in the ground state and

Table 4. Calculated and Experimental Frequency Values of the C−N and C−S Stretching Modes in the Ground and Excited States of **0H**−**3H** by B3LYP Calculations

	0H		**1H**			**2H**		**3H**	
frequency (cm^{-1})	$^1A_1$	$^3A_1$	$^1A'$	$^3A'$	exptl[a]	$^1A'$	$^3A'$	$^1A'$	$^3A'$
ν(C−N)	2153	2394	2149	2345	2106	2142	2341	2135	2339
ν(C−S)	738	712	764	746	788	781	754	795	758

[a] From ref 6.

excited states in gas, ethanol, and water solutions. From Table S6, we can see that the dipole moments of **0H** are apparently increased from ground state to excited state, and the dipole moments of **1H**−**3H** are apparently reduced from ground state to excited state. That is to say, the **0H** should be more stabilized in the excited state by polar solvents than in the ground state, whereas for **1H**−**3H**, their excited states should be more activated by polar solvents than the ground states. Thus, the MLCT/LLCT absorptions of **0H** are red-shifted in ethanol and water with respect to the gas phase, whereas the MLCT/LLCT absorptions of **1H**−**3H** are blue-shifted in ethanol and water with respect to the gas phase. Moreover, the negative solvatochromism in the absorption spectra of the **1H**−**3H** complexes are observed. With the increase of solvent polarity from ethanol to water, the excitation energies are blue-shifted. For instance, in ethanol, the dipole moment of **1H** in the excited state is 3.95 D with a reduction of $\Delta\mu$ = 5.81 D with respect to that in the ground state (9.76 D), whereas in water, the dipole moment of **1H** in the excited state is 2.96 D with a reduction $\Delta\mu$ = 7.76 D with respect to the dipole moment in the ground state (10.72 D). Similarly, the $\Delta\mu$ values of **2H** in ethanol and water are 8.41 and 8.58 D, respectively, whereas the $\Delta\mu$ values of **3H** in ethanol and water are 5.99 and 6.34D, respectively. The increase of $\Delta\mu$ with enhancing solvent polarity from ethanol to water correlates well with the calculated negative solvatochromism.

3.3. Excited-State Structures of 0H−**3H.** On the basis of the optimized ground-state structures, the CIS method is used to optimize the geometry structures of **0H**−**3H** in the excited states, and the four lowest-energy excited states with $^3A_1$, $^3A'$, $^3A'$, and $^3A'$ symmetries, respectively, are obtained. The main geometry parameters of the complexes in the excited state are presented in Table 1. In the lowest-energy excited states, the geometry structures of **0H**−**3H** do not vary notably relative to those in the ground states expect for the Ru−N band distance. The four complexes show a similar variation trend. A general elongation of all the metal–ligand bond lengths is observed. The Ru−N bond distances in the excited state are longer than those in the ground state by 0.04−0.34 Å. Furthermore, the nonmetal bonds (N−C, C−C, and C−O) within tcterpyridine in the triplet excited states are shorter than those in the ground states. The variation of the bond lengths indicate that the electrons are promoted from Ru atom and NCS ligands to tcterpyridine ligands and that the interaction between the Ru atom and ligands is weakened upon excitation. This evidence suggests that a ^{3}MLCT/^{3}LLCT transition should be responsible for the lowest-energy emission.

3.4. Frequencies of 0H−**3H in the Ground and Excited States.** The frequencies of **0H**−**3H** in the ground and excited states were calculated, and the results for C−N and C−S stretching mode are shown in Table 4 together with the experimental IR results for **1H**. From Table 4, we can see the C−N stretching frequency in the ground states appears at 2153 cm^{-1} for **0H**, 2149 cm^{-1} for **1H**, 2142 cm^{-1} for **2H**, and 2135 cm^{-1} for **3H**, which is consistent with the measured data obtained by Grätzel et al.[6] The C−N stretching frequency in the excited states appears at 2394 cm^{-1} for **0H**, 2345 cm^{-1} for **1H**, 2341 cm^{-1} for **2H**, and 2339 cm^{-1} for **3H**. The increase of the C−N stretching frequency in the excited states indicate the strengthening of the C−N bonding interaction, which is consistent with the shortening of the C−N bond distance in the excited states. The C−S stretch frequency in the ground states appear at 738 cm^{-1} for **0H**, 764 cm^{-1} for **1H**, 781 cm^{-1} for**2H**, and 795 cm^{-1} for **3H** and are reduced in the excited states, being in accordance with the lengthening of the C−S bond length in the excited states. The C−S stretch frequencies in the ground states and excited states are increasing from **0H** to **3H**, which is consistent with the decrease of C−S bond distances from **0H** to **3H**.

3.5. Emission Spectra. In view of obtaining the convincing emissive energy, based on the excited-state structures optimized by the CIS method, the emission spectra of complexes **0H**−**3H** in the gas phase and in solution (ethanol and water) are calculated by TDDFT approach at the B3LYP level. The corresponding emissions of **0H**−**3H** are listed in Table 5, associated with the emissive energies, transition assignments, and experimental values.[6] To conveniently discuss the transition property of emission, we present the partial compositions of frontier molecular orbitals related to the emissions in Table 6.

The calculated phosphorescences in ethanol solution for **0H**−**3H** are at 673, 711, 886, and 938 nm, respectively. The phosphorescent emissions are assigned to originate from the ^{3}MLCT/^{3}LLCT excited state. We have presented in the above discussions that the lowest-energy absorptions calculated at 575, 617, 770, and 862 nm for **0H**−**3H**, respectively, also arise from the MLCT/LLCT transition. Since the lowest-energy emissions and absorptions have the same symmetry and transition character for each complex, the phosphorescent emissions should be the reverse process of the lowest-energy absorptions. The Stokes shifts between the lowest-energy absorptions and emissions are 0.32 (**0H**), 0.27 (**1H**), 0.21 (**2H**), and 0.12 eV (**3H**). The small shifts are in agreement with the little change between the ground- and excited-state geometry structures.

The 673 nm emission of **0H** arises from $^3A_1 \rightarrow {}^1A_1$. As shown in Table 5, the emission at 673 nm is mainly from the transitions of MO $21b_1$(LUMO)→MO $20b_1$(HOMO) and MO $21b_1$(LUMO)→MO $39b_2$(HOMO-18) configurations with CI coefficients of 0.72 and 0.20, respectively. According to Table 6, the phosphorescence at 673 nm arises from the

Table 5. Phosphorescent Emission of **0H**−**3H** in the Gas Phase, Ethanol, and Water by TDDFT Calculations, Together with Experimental Values

	medium	transition	config (CI coeff)	E_{nm} (eV)	assignment	exptl (nm)[a]
0H	gas	$^3A_1 \rightarrow {}^1A_1$	$21b_1 \rightarrow 20b_1$ (0.72)	715 (1.73)	^{3}MLCT/^{3}LLCT	
	CH_3CH_2OH	$^3A_1 \rightarrow {}^1A_1$	$21b_1 \rightarrow 39b_2$ (0.20) $21b_1 \rightarrow 20b_1$ (0.72)	673 (1.84)	^{3}MLCT/^{3}LLCT	820
	H_2O	$^3A_1 \rightarrow {}^1A_1$	$21b_1 \rightarrow 20b_1$ (0.72)	670 (1.85)	^{3}MLCT/^{3}LLCT	
1H	gas	$^3A'' \rightarrow {}^1A'$	$32a'' \rightarrow 30a''$ (0.69)	724 (1.71)	^{3}MLCT/^{3}LLCT	
	CH_3CH_2OH	$^3A'' \rightarrow {}^1A'$	$32a'' \rightarrow 30a''$ (0.71)	711 (1.74)	^{3}MLCT/^{3}LLCT	854
	H_2O	$^3A'' \rightarrow {}^1A'$	$32a'' \rightarrow 30a''$ (0.71)	690 (1.80)	^{3}MLCT/^{3}LLCT	829
2H	gas	$^3A'' \rightarrow {}^1A'$	$31a'' \rightarrow 30a''$ (0.25) $32a'' \rightarrow 30a''$ (0.66)	1089 (1.14)	^{3}MLCT/^{3}LLCT	
	CH_3CH_2OH	$^3A'' \rightarrow {}^1A'$	$31a'' \rightarrow 30a''$ (0.18) $32a'' \rightarrow 30a''$ (0.68)	886 (1.40)	^{3}MLCT/^{3}LLCT	900
	H_2O	$^3A'' \rightarrow {}^1A'$	$32a'' \rightarrow 30a''$ (0.69)	798 (1.55)	^{3}MLCT/^{3}LLCT	
3H	gas	$^3A'' \rightarrow {}^1A'$	$32a'' \rightarrow 30a''$ (0.71)	1111 (1.12)	^{3}MLCT/^{3}LLCT	
	CH_3CH_2OH	$^3A'' \rightarrow {}^1A'$	$31a'' \rightarrow 28a''$ (0.26) $32a'' \rightarrow 101a'$ (0.66)	938 (1.32)	^{3}MLCT/^{3}LLCT	950
	H_2O	$^3A'' \rightarrow {}^1A'$	$32a'' \rightarrow 29a''$ (0.71)	845 (1.47)	^{3}MLCT/^{3}LLCT	

[a] From ref 6.

Table 6. Partial Molecular Orbital Compositions in the Lowest-Energy Excited State of **0H**−**3H** in Ethanol by TDDFT Calculations

			compositions (%)				Ru components (%)			
	MO	energy(ev)	Ru	trpy	COO^-	NCS	s	p	d	assignment of orbital
0H	$59a_1$	1.5922	51.4	28.3	0.4	19.8	5.4s	$2.2p_y$	$43.1d_{x^2-y^2}$	$d_{x^2-y^2}$-π*(NCS)
	$44b_2$	1.1965	1.1	90.0	8.9	0.1				π*(terpy)
	$22b_1$	0.5883	0.7	93.2	5.9	0.2				π*(terpy)
	$12a_2$	0.5546	2.6	90.4	6.9	0.0			$2.6d_{xy}$	π*(terpy)
	$11a_2$	−0.4264	1.4	97.3	1.1	0.1			$1.4d_{xy}$	π*(terpy)
	$21b_1$	−0.4762	5.6	88.7	3.7	2.1			$5.5d_{xz}$	π*(terpy)
					HOMO–LUMO Energy Gap					
	$20b_1$	−3.1380	48.8	7.5	0.4	43.2			$48.4d_{yz}$	d_{yz}(Ru)-π*(NCS)
	$10a_2$	−3.1927	51.2	5.3	0.3	43.3			$51.2d_{xz}$	d_{xz}(Ru)-π*(NCS)
	$43b_2$	−3.2991	51.2	14.7	0.4	33.6			$51.0d_{xy}$	d_{xy}(Ru)-π*(NCS)
1H	33a″	−0.4756	0.6	76.8	21.7	1.0				π*(terpy)
	32a″	−1.1889	1.2	98.0	0.7	0.1				π*(terpy)
	31a″	−1.7459	11.3	62.0	24.0	2.6			$11.2d_{yx}$	π*(terpy)
					HOMO–LUMO Energy Gap					
	30a″	−3.6578	32.9	12.2	2.3	52.7			$32.4d_{yz}$	d_{yz}(Ru)-π*(NCS)
	29a″	−3.6698	40.3	3.7	0.2	55.8			$40.3d_{xz}$	d_{xz}(Ru)-π*(NCS)
	101a′	−3.8499	34.9	12.0	0.3	52.8			$34.7d_{xy}$	d_{xy}(Ru)-π*(NCS)
2H	33a″	−1.7086	0.1	93.7	6.1	0.1				π*(terpy)
	32a″	−2.0392	4.9	65.5	29.9	0.6			$2.1d_{xz}$, $2.7d_{yz}$	π*(terpy)
	31a″	−2.4199	11.6	68.2	17.2	3.1			$1.8d_{xz}$, $9.7d_{yz}$	π*(terpy)
					HOMO–LUMO Energy Gap					
	30a″	−4.1228	26.5	12.1	2.0	59.5			$1.5d_{xz}$, 24.6_{yz}	d_{yz}(Ru)-π*(NCS)
	29a″	−4.1487	29.0	5.1	0.7	65.3			$28.2d_{xz}$	d_{xz}(Ru)-π*(NCS)
	101a′	−4.1560	0.3	18.6	80.8	0.3				$p_x/p_y(COO^-)$
	100a′	−4.2847	25.0	10.1	0.6	64.4			$24.8d_{xy}$	d_{xy}(Ru)-π*(NCS)
3H	33a″	−2.3854	1.2	66.8	31.8	0.3				π*(terpy)
	32a″	−2.5944	5.8	79.3	14.7	0.3			$5.7d_{xz}$	π*(terpy)
	31a″	−2.9712	13.7	67.3	13.6	5.3			$13.6d_{yz}$	π*(terpy)
					HOMO–LUMO Energy Gap					
	30a″	−4.5544	19.9	16.0	2.0	62.0			$19.3d_{yz}$	d_{yz}(Ru)-π*(NCS)
	101a′	−4.5846	21.8	3.6	0.5	74.1				d_{xz}(Ru)-π*(NCS)
	29a″	−4.6676	29.9	11.6	0.0	58.5			$29.1d_{xy}$	d_{xy}(Ru)-π*(NCS)
	28a″	−4.8880	1.4	2.0	0.3	96.3			$1.3d_{yz}$	π*(NCS)

^{3}MLCT{tcterpy→d_{yz}(Ru)} combined by ^{3}LLCT(tcterpy→NCS) excited state. The electron density diagrams of the frontier molecular orbitals for the 673 nm emission in Figure 6 intuitivily illustrate the above assignment. Experimentally, the measured phosphorescence of **0H** at 820 nm in ethanol solution has been tentatively assigned to ^{3}MLCT emission.[6]

Similar to the listing for **0H**, the partial frontier molecular orbital compositions of **1H**−**3H** are listed in Table 6. As depicted in Table 6, the unoccupied MOs of **1H**−**3H** are still localized on the tcterpyridine. However, the introduction of COOH group into the terpyridine ligand results in a difference in the compositions of occupied orbitals. In particular, for **2H**, one oxygen lone pair of the carboxylate group (HOMO-2) inserts into the three Ru(d)-NCS MOs. It is interesting to note that, in the Ru(d)-NCS character HOMOs, the contributions of d (Ru) are decreasing from **0H** to **3H** (see Table 6). The similar difference has been observed from the absorption spectra of **0H**−**3H**. The nature of the phosphorescence of **1H** and **2H** isare similar to that of **0H** (see Table 5 and Figure 6). The 711 and 886 nm phosphorescence for **1H** and **2H**, respectively, derived from the $^3A' \rightarrow {}^1A'$ transition, are attributed to tcterpyridine→d_{yz}(Ru)/

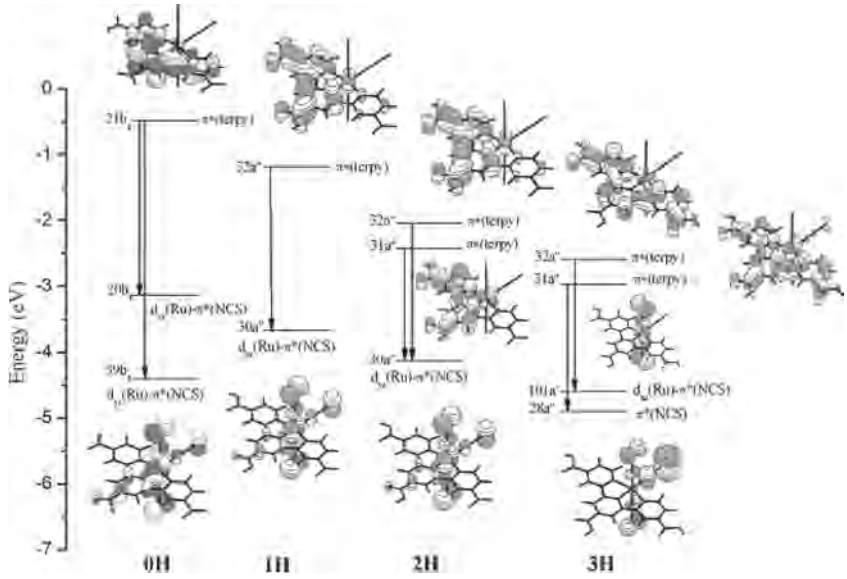

Figure 6. Transitions responsible for the emissions at 673, 711, 886, and 938 nm for **0H**, **1H**, **2H**, and **3H**, respectively, simulated in ethanol medium.

NCS charger transfer (^{3}MLCT/^{3}LLCT) transition. For complex **3H**, the 938 nm emission in the ethanol solution has the nature of $^3A' \rightarrow {}^1A'$ transition. The phosphorescence is mainly from the transitions of MO 32a″(LUMO+1)→MO 101a′(HOMO-1) and MO 31a″(LUMO)→MO 28a″(HOMO-3) configurations with CI coefficients of 0.66 and 0.26, respectively. From Table 6 and Figure 6, the MO 31a″ and MO 32a″ are both localized on the tcterpyridine fragments. The MO 101a′ is composed of 22% Ru(d_{xz}), 74% NCS ligands, and 4% tcterpyridine ligand, whereas the MO 28a″ is localized on the three NCS ligands up to 96% in composition. Therefore, the 938 nm emission of **3H** can be described as tcterpyridine→d_{xz}(Ru)/NCS charge transfer (^{3}MLCT/^{3}LLCT) transition involving a few ^{3}LMCT transitions. The electron density diagrams of the emissions for **1H**−**3H** are illustrated in Figure 6 to help us rationalizing the transitions better. Experimentally, the emissions of **1H**−**3H** have been assigned to originate from the Ru(tcterpy)CT excited state.[6]

The molecular orbital energy levels of **0H**−**3H** are used to describe the protonation effects on phosphorescent emission. The HOMO–LUMO energy gaps for **0H**−**3H** decrease in the order 2.66 eV (**0H**) > 1.91 eV (**1H**) > 1.70 eV (**2H**) > 1.58 eV (**3H**), with the increasing number of COOH groups. Moreover, the introduction of COOH groups causes a red shift of phosphorescent emission on going from **0H** to **3H**. The red shift of the emission from **0H** to **3H** is due to the lower π^*(tcterpyridine) orbital in the protonated forms compared to the deprotonated form.[39]

To check the solvent effect on phosphorescent emission, we also calculated the emissions of **0H**−**3H** in the gas phase, ethanol, and water by the TDDFT and TDDFT/CPCM methods, respectively. The calculated phosphorescent emissions of the **0H**−**3H** complexes in gas, ethanol, and water are summarized in Table 5. It is evident that the emission spectra in solutions are in considerably better agreement with the experimental than the emission spectra computed in the gas phase. The phosphorescences for **0H**−**3H** in the gas phase and water solution are similar to those of **0H**−**3H** in ethanol solution and also have ^{3}MLCT/^{3}LLCT character. In addition, in water the emissions for **0H**−**3H** are all blue-shifted compared to those in ethanol solution, because the ability to form a hydrogen bond between the water molecule and the lone pair electrons on the sulfur of the NCS ligands is stronger than that of the ethanol molecule.

4. Conclusions

Electronic structures and spectroscopic properties of **0H**−**3H** are investigated theoretically. We predict the absorption and emission spectra in the gas phase and solution using the TDDFT method without and with the solvent-effect CPCM model, respectively. Taking into account the protonation effect and solvent effect, the following conclusions can be drawn.

The analysis of the electronic structures for **0H**−**3H** shows that the higher occupied MOs are mainly composed of Ru d orbitals and thiocyanate ligands and the lower unoccupied MOs are the admixture of π^* orbitals localized on the terpyridine ring ligands and the carboxylic groups. These thiocyanate and carboxylic group contributions to the HOMOs and LUMOs, respectively, are believed to play an important role in the regeneration and electron injection performance of dye-sensitized TiO_2 solar cells. Moreover, the protonation effect leads to a sizable difference in the electronic structures. In the cases of both absorption and emission, the energy level of HOMOs and LUMOs for **0H**−**3H** decrease obviously with the introduction of the COOH groups. For each step of protonation, the stabilization of the unoccupied orbitals is larger with respect to the occupied orbitals. Thus, the HOMO–LUMO gap of absorptions and emissions both decrease from **0H** to **3H**.

The calculated lowest-energy MLCT/LLCT absorptions for **0H**−**3H** complexes are at 575, 617, 770, and 862 nm,

(39) Baribelletti, F.; Flamigni, L.; Guardigli, M.; Sauvage, J.-P.; Collin, J.-P.; Sour, A. *Chem. Commun.* **1996**, 1329.

respectively. The red shift of the longer wavelength band as the number of COOH groups increases is mainly due to the stronger electron-withdrawing nature of the carboxylic acid groups compared to the carboxylate anions onto the terpyridine ligand.

Inclusion of the solvent leads to important changes of the energies and composition of the molecular orbitals of the complexes; as a consequence, the spectra calculated in solution are in good agreement with the experiment. And the absorption spectra of the full deprotonated form (**0H**) are red-shifted in ethanol and water with respect to the gas phase. On the other hand, in the protonated complexes (**1H**−**3H**), the absorption band are blue-shifted in ethanol and water with respect to the gas phase. Furthermore, the negative solvatochromism in the absorption spectra of the **1H**−**3H** complexes are observed. With increasing solvent polarity from ethanol to water, the excitation energies are blue-shifted. The appearance of negative solvatochromism is closely related to a negative change of dipole moment in the excited state with respect to the ground state, which results in a higher stabilization of the ground state in solvents with increasing polarity.

The calculated lowest-energy phosphorescence in ethanol solution for **0H**−**3H** are at 673, 711, 886, and 938 nm, respectively. We attribute them to tcterpyridine→d(Ru)/NCS charge transfer (^{3}MLCT/^{3}LLCT) transitions.

Acknowledgment. This work is supported by the Natural Science Foundation of China (20173021, 20333050, 20573042, and 20703015) and the Natural Science Foundation of Heilongjiang Province of China (B200601).

Supporting Information Available: Energy levels of **0H**−**3H** in gas phase, ethanol, and water under TDDFT calculation; molecular orbital compositions of **1H**−**3H** in ethanol and of **0H**−**3H** in gas phase and water; calculated absorptions of **0H**−**3H** in gas phase and water; and calculated dipole moments of the ground states and excited states of **0H**−**3H** in the gas phase, ethanol, and water. This material is available free of charge via the Internet at http://pubs.acs.org.

IC070139B